5-2016

Cryostat System for Spacecraft Materials Testing

Justin Dekany

CRYOSTAT SYSTEM FOR SPACECRAFT MATERIALS TESTING

by

Justin Dekany

A thesis submitted in partial fulfillment
of the requirements for the degree

of

MASTER OF SCIENCE

in

Physics

Approved:

_____	_____
J. R. Dennison, Ph.D. Major Professor	Vince Wickwar, Ph.D. Committee Member
_____	_____
Farrell Edwards, Ph.D. Committee Member	Mark R. McLellan, Ph.D. Vice President for Research and Dean of the School of Graduate Studies

UTAH STATE UNIVERSITY
Logan, Utah

2016

ABSTRACT

Cryostat System for Spacecraft Materials Testing

by

Justin Dekany, Master of Science

Utah State University, 2016

Major Professor: Dr. J. R. Dennison
Department: Physics

The main cause of spacecraft failures is due to the harsh space environment; therefore, rigorous testing of materials used in modern spacecraft is imperative to ensure proper operation during the life span of the mission. Enhancing the capabilities of ground-based test facilities allows for more accurate measurements to be taken as it better simulates the environment to which spacecraft will be exposed. The range of temperature measurements has been significantly extended for an existing space environment simulation test chamber used in the study of electron emission, sample charging and discharge, electrostatic discharge and arcing, electron transport, and luminescence of spacecraft materials. This was accomplished by incorporating a new two-stage, closed-cycle helium cryostat, which has an extended sample temperature range from <40 K to >450 K, with long-term controlled stability of <0.5 K. The system was designed to maintain compatibility with an existing ultrahigh vacuum chamber (base pressure $<10^{-7}$ Pa) that can simulate diverse space environments. These existing capabilities include controllable vacuum and ambient neutral gases conditions ($<10^{-7}$ to 10^{-1} Pa), electron fluxes (5 eV to 30 keV monoenergetic, focused, pulsed sources ranging from 10^{-4} to 10^{10}

nA-cm^{-2}), ion fluxes (<0.1 to 5 keV monoenergetic sources for inert and reactive gases with pulsing capabilities), and photon irradiation (numerous continuous and pulsed monochromatic and broadband IR/VIS/UV [0.5 to 7 eV] sources). The original sample mount accommodates one to four samples of 1 cm to 2.5 cm diameter in a low-temperature carousel, which allows rapid sample exchange and controlled exposure of the individual samples. Multiple additional sample mounts have been added to allow for standalone use for constant voltage measurements, radiation induced and conductivity tests, as well as extended capabilities for electron-induced luminescent measurements to be conducted using various material sample thicknesses in the original existing space environment simulation test chamber.

(43 pages)

PUBLIC ABSTRACT

Cryostat System for Spacecraft Materials Testing

Justin Dekany, Master of Science

Utah State University, 2016

An existing space environment simulation test chamber used in the study of electron emission, sample charging and discharge, electrostatic discharge and arcing, electron transport, and luminescence of spacecraft materials now has extended temperature control capabilities. By incorporating a two-stage, closed-cycle helium cryostat, it is now possible to simulate the temperature typical spacecraft will experience when in orbit, ranging from <40 K to >450 K. The system was designed to maintain compatibility with an existing ultrahigh vacuum chamber that can simulate diverse space environments. This vacuum chamber can simulate space environment conditions by producing the same pressure, amount of electrons, electromagnetic radiation and temperature a typical satellite may experience when in orbit. For testing, multiple cameras are positioned to view the spacecraft sample to measure the amount of light that may be emitted from the sample. This is important, especially for space-based optical observatories where light contamination is of concern. The cryostat system can also be adapted for use in other test facilities, as well as in a standalone configuration for specific tests that involve low-temperature electronic conductivity tests.

ACKNOWLEDGMENTS

I would like to express my sincere gratitude and thanks to my advisor Dr. J.R. Dennison. I would like to thank you for the opportunity to conduct this research and for allowing me to grow as a research scientist. Your advice, encouragement, and immense knowledge are greatly appreciated.

I would also like to give my sincere thanks to my committee members, Dr. Farrell Edwards and Dr. Vince Wickwar for their support and help in getting this work completed. I am thankful for their aspiring guidance, invaluably constructive criticism, and advice.

I would like to thank the USU Physics Department. You all have been wonderful to work with and the Department Head, Jan Sojka, has done more for me than I can say. For that I thank you.

Through the years, I have worked closely with many undergraduate and graduate students and have learned a lot from all of them. Your support and willingness to help me have been greatly appreciated. In particular, I would like to thank Ryan Hoffmann for teaching me the ropes and supporting me as a friend. This work would not have been possible without the help from Greg Wilson and Amberly Jensen. Both have succeeded greatly in their endeavors, and as a team, we accomplished a significant amount of ground-breaking research. I greatly value their friendship and I deeply appreciate their belief in me.

Lastly, I would like to thank my family. I am grateful to my parents and mother-in-law for their encouragement and moral support as I worked my way through this venture. I would also like to thank my friends who believed in me, supported me, and

kept me going when I needed it most. And finally to my loving, supportive, and patient wife, Julie, and daughter, Jemma, I want to thank you for listening to my science talk, for cheering me on, and for always standing by me. I could not have done it without you.

Justin Dekany

CONTENTS

Page

LIST OF FIGURES

Figure Page

LIST OF SYMBOLS

$\dot{D}$ = dose rate.

$\dot{D}_{sat}$ = saturation dose rate.

E_{inc} = incident beam energy.

I_{γ} = cathodoluminescence intensity.

J_{inc} = incident beam current density.

k_B = Boltzmann's constant.

L = material thickness.

$Q_{e\gamma}$ = average conversion efficiency of excited electrons to photons.

q_e = electron charge.

$R(E_{inc})$ = energy-dependent range.

T = temperature.

ε_{ST} = energy depth of the shallow traps below the conduction band.

$\eta(E_{inc})$ = energy-dependent backscattered electron yield.

λ = wavelength.

ρ_m = material mass density.

LIST OF ABBREVIATIONS

AFRL	Air Force Research Laboratory.
CCD	Charge Coupled Device.
CL	Cathodoluminescence.
CVC	Constant Voltage Conductivity.
ESD	Electrostatic Discharge.
FC	Faraday Cup.
HV	High Voltage.
JWST	James Webb Space Telescope.
MPG	Materials Physics Group.
MSFC	Marshall Space Flight Center.
RIC	Radiation-Induced Conductivity.
SEMM	Space Environment Effects Materials.
SLR	Single Lens Reflex.
UHV	Ultrahigh Vacuum.
USU	Utah State University.

CHAPTER 1

INTRODUCTION

This thesis presents the modifications to a closed-cycle helium refrigerator unit to allow for materials testing at cryogenic temperatures in various ultrahigh vacuum (UHV) space-environment test chambers.

In this modern age of technology, spacecraft have become more sophisticated and capable than ever before, in large part due to advancements in new materials used to construct these modern marvels. With new materials being created every day, the need for testing these materials to ensure optimum functionality greatly impacts the success of the mission. Although the quality of instrument parts has improved over the years, the main cause for spacecraft failure is still due to the interaction with the space plasma environment (Leach and Alexander, 1995). With missions extending further into space, such as the James Webb Space Telescope (JWST), which will orbit the L2 Lagrange point at 1.5 million km from Earth, there is no possibility of a repair mission to fix any problems. Testing the materials used in these spacecraft using space-simulation test chambers configured to mimic the actual conditions the craft will undergo during normal operational and worst-case solar storm conditions allows designers to generate better models to predict and mitigate possible failures.

The Utah State University (USU) Materials Physics Group (MPG) designed a cryostat apparatus (Dekany *et al*., 2014) to aid NASA in testing materials in a simulated low-temperature space environment. The cryostat decreases the temperature of the test samples to temperatures the JWST will experience while in orbit; this system can be used in a variety of space-environment test chamber configurations. During the course of

these experiments, it became apparent there was additional concern for the usability of some material. Polymers and some optical coatings exhibit cathodoluminescence (CL) (Jensen *et al*., 2014b), a phenomenon not expected, nor welcome, in an open-architecture space observatory (Jensen *et al*., 2013b). By conducting these tests in a controlled laboratory environment, it was possible to calibrate the detectors *in situ*, with help from the Space Dynamics Laboratory, to obtain absolute spectral radiance measurements. These tests have helped mitigate potential issues with the JWST once in orbit.

This thesis will discuss the modifications made to a closed-cycle helium refrigerator unit, which made it possible for these critical low-temperature tests to be made. Chapter 2 gives an overview of the electron emission test chamber and addresses the modifications to the closed-cycle helium refrigerator unit, which in its completed state is referred to as the cryostat apparatus. This unit was originally designed to work with a specific UHV chamber, whose capabilities are described in some detail, followed by a discussion of the three main sample mounting attachments, which allow for various sample size and experimental capabilities. Details of the wiring and insulation used to take full advantage of the low temperatures the cryostat can achieve will also be discussed.

Chapter 3 describes some of the many different materials that have been tested at USU using the MPG electron emission test chamber and the different mounting configurations needed to test these materials. Included is a discussion of the tests conducted at the Air Force Research Laboratory (AFRL) at Kirtland Air Force Base, where the cryostat unit was transported to conduct high-energy electron bombardment Radiation-Induced Conductivity (RIC) tests on thin film glass materials. As a final point

of comparison, tests conducted at NASA's Marshall Space Flight Center (MSFC), which used actual JWST onboard materials tested under similar conditions to experiments conducted at USU, were performed to confirm the validity of the cryostat's performance.

Finally, Chapter 4 contains conclusions related to the test apparatus. There is a summary of the efforts made to ensure proper operation of the cryostat unit. Lastly, a discussion of future work utilizing the cryostat at USU to extend the capabilities to include additional electron transport experiments is presented.

CHAPTER 2

INSTRUMENTATION

This chapter discusses the modifications made to the cryostat apparatus. It was designed to maintain continuous control of sample temperature and has been adapted to various UHV chambers, which allows for a wide range of electron flux and energy bombardment testing. Details of the three main sample holders specifically designed for a multitude of experimental tests on spacecraft materials will also be described. Throughout this chapter, all letter references A-Y refer to the list in FIG. 2.3 and in specific images when stated.

2.1. Electron Emission Test Chamber

A closed-cycle helium refrigerator unit has been modified to allow for the attachment to a space environment electron emission test chamber (Nickles, 2002; Chang *et al*., 2000) (FIG. 2.1). The test chamber uses standard mechanical and turbomolecular pumps (V) for roughing and an ion pump (W) for continuous maintenance-free operation (base pressure of $<10^{-7}$ Pa). Absolute pressure is monitored with Convectron and ion gauges (X). Partial pressure is measured with a residual gas analyzer (Y). Electron flux is produced with a high-energy gun (Kimball, Model EGPS-21B) (A), which provides a monoenergetic beam with a flux of ~1pA/cm^2 to 1 μA/cm^2 over an energy range of 5.00 to 30.00±0.01 keV. For experiments described here, a continuous beam mode was used, with a broad defocused beam of ~2 cm diameter FWHM; focused, pulsed beams are also possible (Hoffmann and Dennison, 2012). The current is monitored in real time using an *in situ* Faraday cup (FC) (G) located in the center of the sample mount (D). Currents are

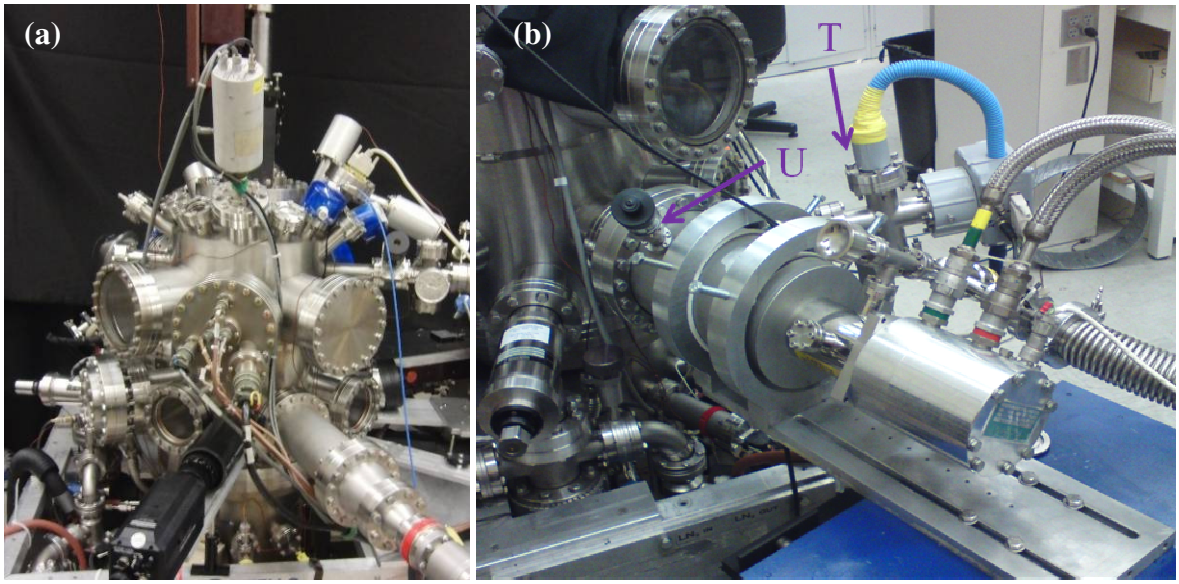

FIG. 2.1. Electron Emission Test Chamber. (a) Electron emission test chamber at USU. (b) Closed-cycle helium refrigerator unit attached to the electron emission test chamber.

measured using fast, sensitive picoammeters with <0.2 pA resolution (Thomson *et al*., 2003). Additional lower-energy electron gun sources (5 eV to 5 keV), ion sources (100 eV to 5 keV), and photon sources (~150 nm to 2000 nm) are also available in the chamber (Dennison, 2009).

Light detection uses several cameras calibrated *in situ* using NIST traceable methods, allowing for absolute spectral radiance values to be obtained. The cameras are positioned with clear views of the sample through vacuum port windows; this allows collection of photon emission data resulting from electron-induced CL and arcing (Jensen *et al*., 2014b). A Single Lens Reflex (SLR) Charge Coupled Device (CCD) camera (O) (Cannon, EOS Rebel XT DS126071; ~400 nm to 700 nm) captures 10 Mpixel visible light images at 30 s shutter speeds and full aperture with a 55 mm lens, giving it an average spectral response of ~$4 \cdot 10^9$ counts/(W/cm^2·sr·μm). An image-intensified CCD

video camera (L) (Xybion, ISG-780-U-3; ~400 nm to 900 nm) collects data at 30 frames per second and using a 55 mm lens had a spectral response of ~$4 \cdot 10^{10}$ counts/ ($W/cm^2 \cdot sr \cdot \mu m$). An InGaAs video camera (M) (Goodrich SU320MX-17RT; 800 nm to 1700 nm) is operated at ambient room temperature collecting data at 60.1 frames per second. It has a spectral response of ~$1 \cdot 10^9$ counts/ ($W/cm^2 \cdot sr \cdot \mu m$) using a 35 mm lens. An InSb video camera (N) (Santa Barbara Focalplane SBF180), operating at liquid nitrogen temperatures, acts as a low spatial resolution mid-IR detector. The photon response of this detector increases in sensitivity with increasing wavelength ranging from 1 μm to 5.5 μm at varying integration times (~10 Hz to ~30 Hz) depending on the band pass filter used; it has a spectral responsivity of ~$7 \cdot 10^7$ counts/($W/cm^2 \cdot sr \cdot \mu m$).

Two fiber optics-based spectrometers (K) provide Ultraviolet/Visible/Near Infrared photon spectral measurements from ~250 nm to 1700 nm. The UV/VIS spectrometer (Stellarnet, 13LK-C-SR; ~200 nm to 1080 nm) has a wavelength resolution of ~1 nm, while the NIR spectrometer (Stellarnet, RW-InGaAs-512; ~1000 nm to 1700 nm) has a ~3 nm resolution. Both detectors are housed in a Peltier cooler, which maintains -20 K from ambient. A 4 cm diameter MgF collection optic focuses the emitted light into a 1 μm fiber optic cable routed to the spectrometers (Jensen and Dennison, 2015).

2.2. Low-Temperature Stage Design

A cryostat apparatus has been added to the space environment simulation chamber to extend the operational temperatures for sample testing from <40 K to >450 K. Temperature is maintained to ±0.5 K using a standard computer-controlled PID

temperature controller (RMC Cryosystems CR31-21) under Labview™ command and platinum RTDs (I) mounted on the sample holder, low-temperature stage, and cryostat radiation shield. A large mass radiation shield (J) is attached to the cryostat's first stage (thermal load capacity of ~10 W at ~80 K) and a sample mounting stage is attached to the cryostat's second stage (thermal load capacity of ~1 W at ~20 K); these large thermal masses help maintain a constant sample temperature. Due to radiative heat transfer from the chamber walls, the addition of a multilayer thermal insulation blanket (R) wrapped around the first stage radiation shield (J) is required. This blanket consists of five sheets of thin conducting material separated by a thin mesh of insulating material. With this addition to the apparatus, the sample holder, which is mounted to the cryostats second-stage sample pedestal (B) can reach <40 K, a temperature comparable to passively cooled spacecraft in standard orbit. Direct measurement of a sample confirmed a <2 K gradient between the samples and sample holder on which the temperature probe is mounted. Once the chamber is down to pressures of $<5 \cdot 10^{-3}$ Pa, the cryostat cools the sample at a rate of ~ 1 K/min, reaching the lowest temperature of ~40 K in about 4 hours (FIG. 2.2); this temperature can be sustained for weeks. Heating the sample is accomplished using a combination of control and bulk heaters attached to the radiation shroud and sample mount. Once activated, the temperature controller can heat the sample at a rate of ~ 1.5 K/min and can maintain intermediate temperatures from <40 to > 450 K. FIG. 2.2 shows a typical cooling and heating profile. The cryostat [FIG. 2.3(b)] can be removed from the electron emission chamber and installed on other vacuum chambers that have an available 10 cm or 15 cm port.

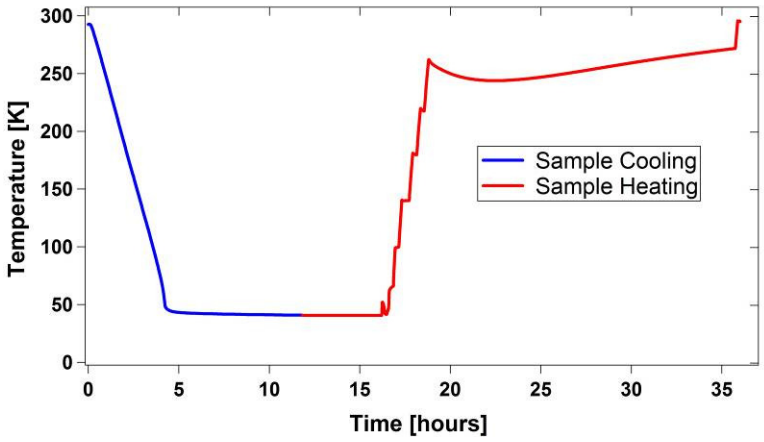

FIG. 2.2. Typical sample stage cooling and sample heating curves, with multiple sustained temperatures shown during heating cycle.

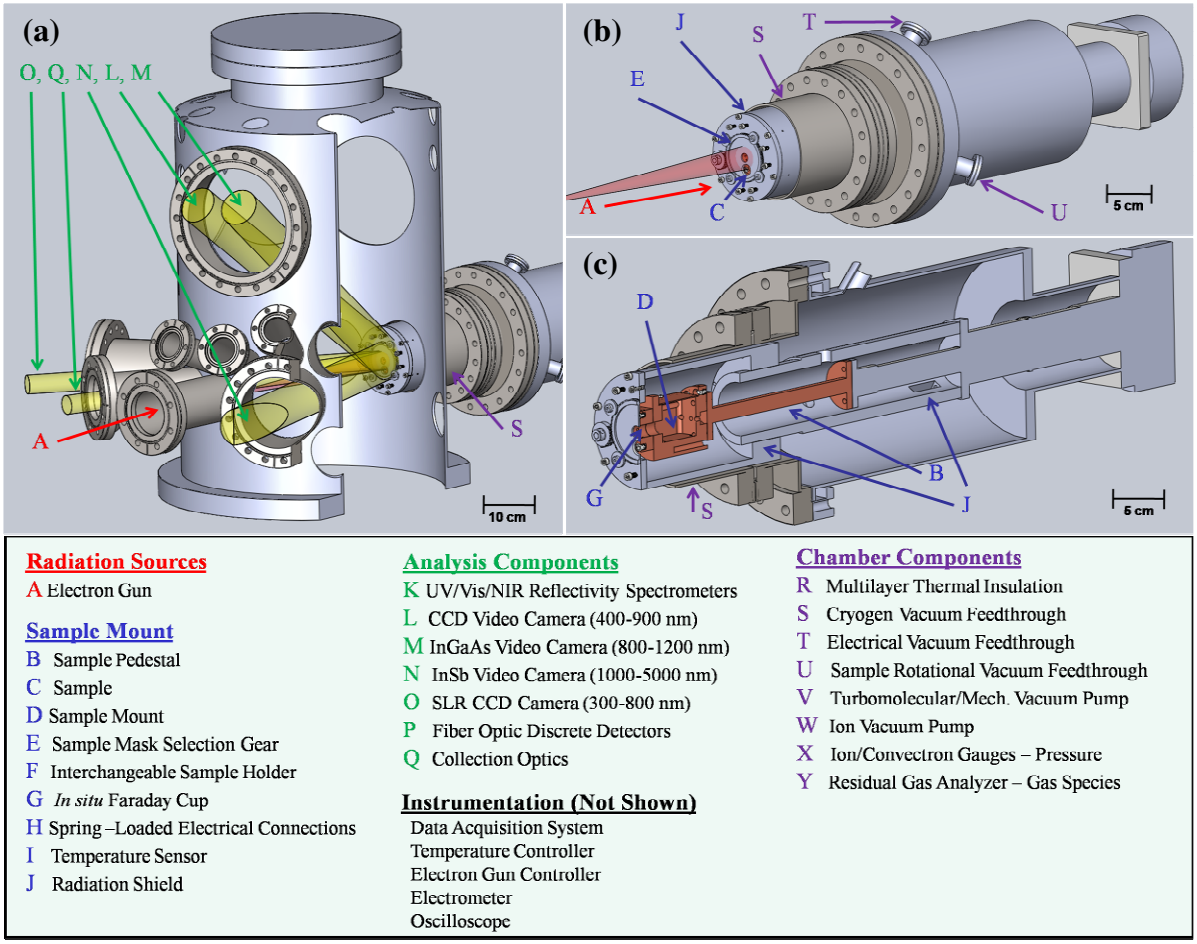

FIG. 2.3. Experimental test chamber. (a) Chamber exterior view with cutaway showing the various analysis component lines of sight. The electron gun is positioned on axis with the sample plane. (b) Cryostat chamber mount, showing the electron beam trajectory (red). (c) Cutaway view of cryostat showing the first stage radiation shroud and second low-temperature stage, with sample mount and pedestal (red).

2.3. Sample Stage Design

The original design for the cryostat sample holder was for test coupons that were either 1 cm or 2.5 cm diameter. Tests using such samples involved electron-induced CL, where the sample face must be easily viewed from multiple port windows at various incident angles. This initial requirement set the basis for connecting samples to the cryostats cold finger. In addition to CL measurements, multiple sample stages have been designed to allow for RIC and constant voltage conductivity (CVC).

2.3.1. CL Mount

The sample mount (D) has a versatile design that allows for a variety of configurations and sample sizes. Multiple sample holders (F) can be quickly interchanged with the use of spring-loaded, electrically-isolated electrode connectors (H), as shown in FIG. 2.4. The sample stage is electrically isolated with a Kapton^{TM} spacer and PEEK screws, but maintains good thermal contact with the sample stage. The sample stage has a large wiring cavity (D) to facilitate various low-noise electrical connections, in addition to allowing room for bulk and control heaters.

In one configuration, four 1 cm diameter samples can be installed with an optional *in situ* FC (G) in the center location allowing for real-time monitoring of electron beam current [FIG. 2.5(a)]. Samples in this configuration are mounted on (10.0 ± 0.1) mm diameter Cu cylinders, usually using UHV compatible, low-temperature, conductive epoxy (Masterbond, EP21TDCS-LO). The Cu cylinders are mounted in sample blocks using ceramic pins or 100 μm diameter sapphire spheres held in place with set screws to provide electrical isolation [FIG. 2.5(a)]. Electrical connections to the sample are made

via one or more spring-loaded pins from the rear, allowing the sample current(s) to be monitored. Using this configuration, a sample mask selection gear (E) coupled to an external rotation translation feed through (U) allows masking of the samples not being tested [FIG. 2.6(a)]; this minimizes potential sample charging of these samples. The sample mask also minimizes the amount of sample area exposed to the higher temperature chamber walls, since the mask is attached to the 80 K second stage of the cryostat. Larger samples of up to 2.5 x 2.5 cm square can be tested using a different sample mount (F), as shown in FIG. 2.6(b).

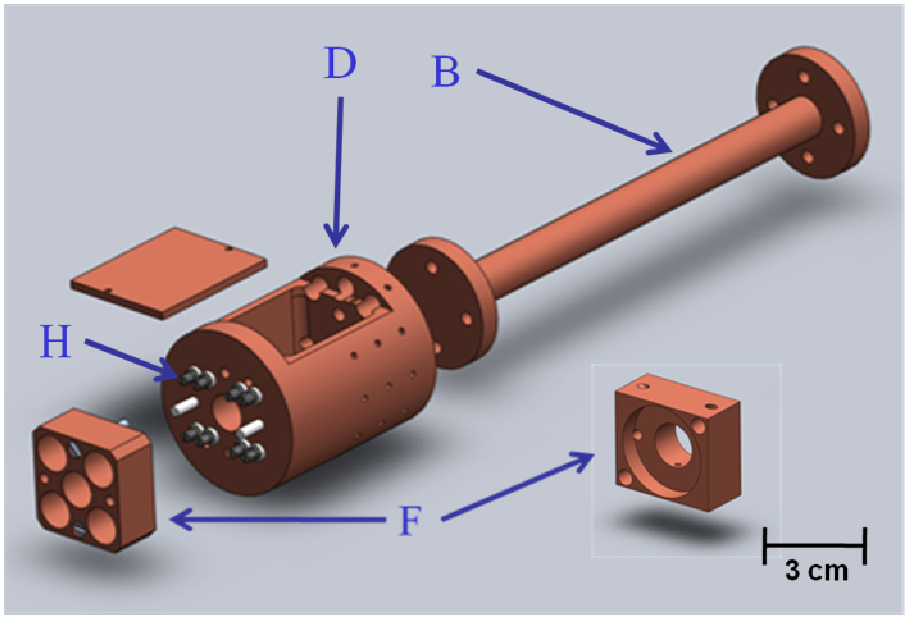

FIG. 2.4. Cold finger sample mount. (a)View of cryostat's first stage sample pedestal and interchangeable sample holder, which attaches to the cryostat. Shown is a sample holder for four 1 cm diameter samples and a single 2.5 cm diameter sample.

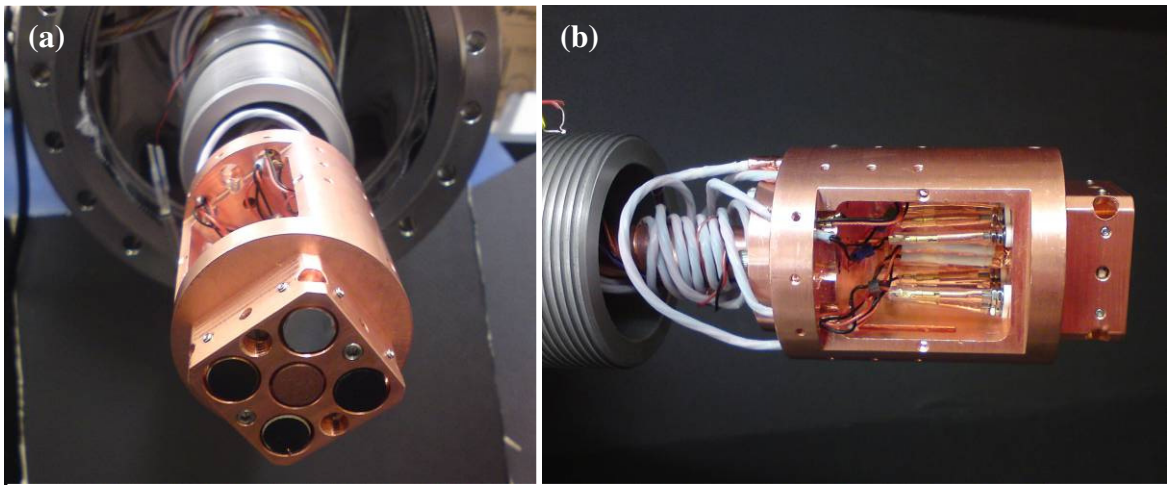

FIG. 2.5. CL sample stage and wiring. (a) View of four 1 cm diameter samples attached to the sample stage and a central Faraday cup. (b) Wiring for electrical connections is coiled around the sample pedestal to reduce the thermal load from external connections.

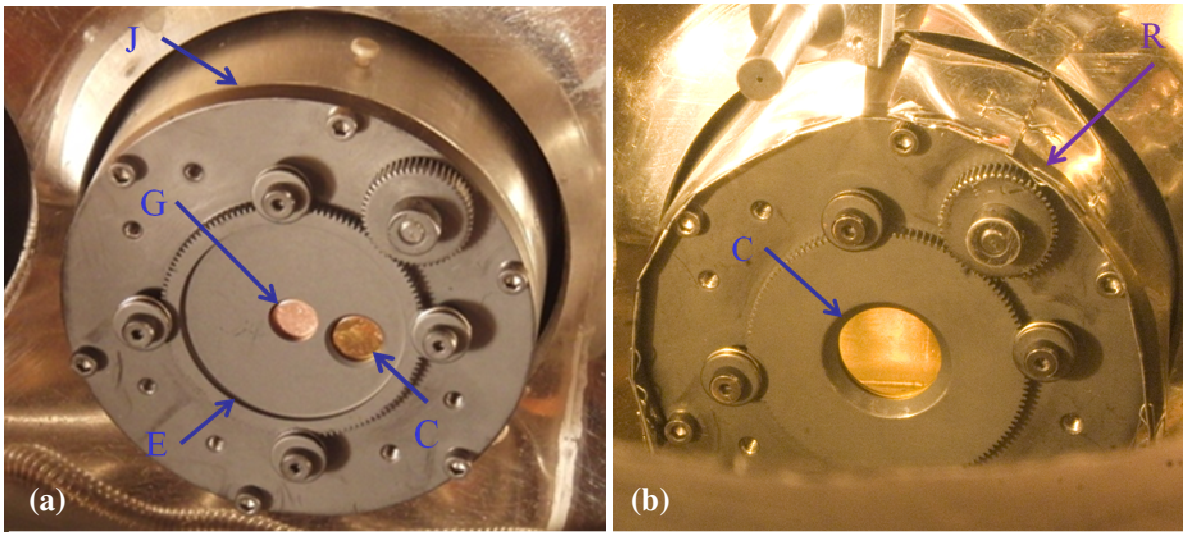

FIG. 2.6. Sample Carousel Design. (a) Sample selection gear controlled using an external rotation translation (U). The gear/sample mask to access the Faraday cup (G) and one of four 1 cm diameter samples is shown. (b) Face plate with a 2.5 cm diameter sample mounted. Note radiation blanket wrapped around first stage radiation shield (J) of cryostat.

2.3.2. RIC Mount

The cryostat system was moved to AFRL at Kirtland Air Force Base and was used to conduct high-energy, ~50 keV, electron bombardment RIC tests on thin-film glass materials (Dennison *et al*., 2016; Hoffmann *et al*., 2013). Due to the fragile nature of these thin films, (24 x 24 mm and 0.2 mm thick), a mount was designed to allow for the samples to be securely mounted to the existing 1 cm diameter sample holder. Although the mount was initially designed to conduct electrical conductivity tests, the RIC mount has been modified to allow for CL test (Jensen, 2014) as well as surface potential measurements on thicker ceramic samples (Guerch *et al*., 2015) by employing adjustable spring mounts to the outermost plate (FIG. 2.7).

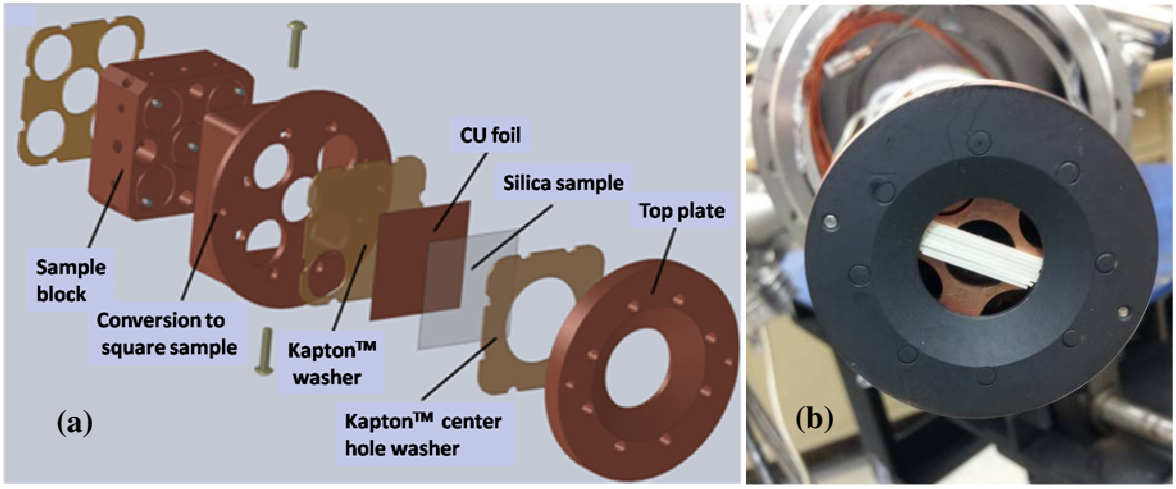

FIG. 2.7. RIC attachment. (a) Modified for CL tests at USU testing-thin-film fused silica (disordered SiO_2). (b) 2 mm thick ceramic samples adapted to the RIC mount for low-temperature surface potential tests.

2.3.3. CVC Mount

USU houses a dedicated CVC chamber with cooling capabilities down to ~150 K using liquid nitrogen (Dekany *et al*., 2014). Many tests have been conducted using this chamber, and have indicated the need for even lower temperatures. For this reason, a mount that attaches directly to the cryostat sample mount, which allows for standalone operation to conduct temperature controlled CVC measurements, has been developed. This sample stage is designed for testing of a single circular sample up to 2.5 cm diameter and 1 mm thick, although it is possible to adapt the mount to slightly thicker samples if necessary. In order to manage the high voltage (HV), up to 5 kV, an additional HV feedthough has been added to the cryostat; the sample mount ground and voltage leads must be rewired to the HV lines (FIG. 2.8).

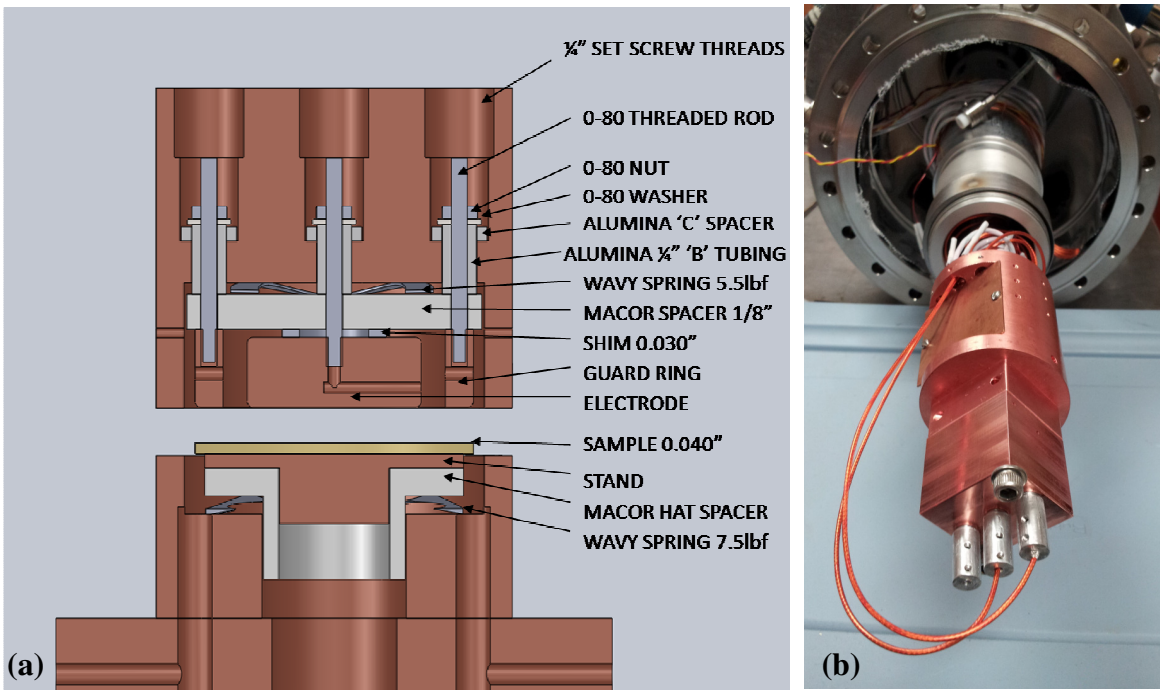

FIG. 2.8. CVC attachment. (a) Solid model of the CVC mount components and assembly order. (b) CVC mount attached to the cryostat with coaxial insulated high-voltage leads and aluminum ground caps for noise reduction.

CHAPTER 3

MATERIALS TESTING

This chapter begins with an overview of the various samples studied and a brief description of how the materials are used in spacecraft. A summary of the various facilities where the material samples were tested is also presented. A model to describe the CL phenomena to quantify the results of these tests is given, which allows for a quantitative analysis of the impact these materials may have on specific spacecraft designs. The chapter ends with a comparison of the test results for many of the materials.

3.1. Material Samples

Numerous materials have been tested with the cryostat apparatus. The samples were largely supplied by NASA; some are made of typical materials used in modern spacecraft construction and others are specific to more advanced space-based observatories, such as the JWST. Initial tests conducted at USU for common spacecraft materials focused on conductivity and electron transport experiments (Dekany *et al*., 2013). As these tests continued, it became clear that some materials exhibited some detectable level of CL (Dennison *et al*., 2012), which opened the door for a more extensive investigation into this phenomenon (Jensen, 2014; Jensen and Dennison, 2014a).

3.1.1. Amorphous Polymers

A variety of polymers have been tested by the USU MPG. These materials are used extensively in spacecraft construction. Kapton™ and low-density polyethylene are

typically used as lightweight insulation for wires, for large-scale instrumentation insulation, and is a main component in the JWST solar insulation shield (Dekany *et al*., 2015). For use in more structural applications, nanodielectric carbon-loaded polyimide (Jensen *et al*., 2013a) is used. The addition of the carbon nanoparticles is to allow the polyimide to be less conductive, reducing the chance of electron charging, which may result in catastrophic failures due to electrostatic discharge. Cynate ester/graphite fiber composites (Roth *et al*., 2009), and bisphenol/amine epoxy (Dennison *et al*., 2013; Dekany *et al*., 2015) are typically used to reinforce spacecraft structures. All of these materials have shown various levels of CL. Understanding the levels of light contamination is critical when designing modern spacecraft with optical capabilities.

3.1.2. Fused Silica

Fused silica optical coatings (SiO_2) (Jensen and Dennison, 2015) are used to protect the reflective surfaces of observational mirrors. Understanding the level of CL from these coatings is important in open architecture space-based observatories due to the amount of exposure to the space plasma environment these structures will undergo. Since most of these coatings are very thin, the amount of light emission from these materials is minimal and hard to measure; for this reason it is necessary to obtain accurate measurements of the coating's performance for calibration purposes.

3.1.3. Ceramics

Ceramic materials, including boron nitride (BN) and annealed aluminum oxide, (Al_2O_3) have been tested at low temperatures (Guerch *et al*., 2015). These materials are rigid and are used in a variety of places throughout a spacecraft due to their radiation

resistance. By annealing the ceramics, the conductivity of the outer surface of the ceramic can be reduced to limit the chance of Electrostatic Discharge (ESD).

3.2. Model of CL Intensity

The model developed for the observed electron-induced luminescence phenomenon is based on band theory of highly disordered insulating materials (Jensen and Dennison, 2015; Teyssedre *et al*., 2001; Sim and Dennison, 2013). The observed luminescence occurs when an incident high-energy, charged particle undergoes a series of inelastic collisions exciting valence-band electrons into the conduction band. The excited electrons rapidly decay to localized (shallow trapped) states, with a mean binding energy ε_{ST} below the mobility edge. A final electron transition, from the short-lived shallow trap states to longer-lived deep trap states, is the origin of the emitted photon. The model predicts that I_γ scales with incident current density J_{inc}, incident beam energy E_{inc}, temperature T, and emitted photon wavelength λ as

$$I_\gamma\left(J_{inc}, E_{inc}, T, \lambda; \varepsilon_{ST}, \dot{D}_{sat}\right) \propto$$

$$\left[\frac{\dot{D}(J_{inc},E_{inc})\dot{D}_{sat}}{\dot{D}(J_{inc},E_{inc})+\dot{D}_{sat}}\right]\left\{\rho_m Q_{e\gamma}(\lambda,T)\left[1-e^{-(\varepsilon_{ST}/k_BT)}\right]\right\}$$

$$\times\begin{cases} R(E_{inc}) \;;\; 0 \le R(E_{inc}) \le L, & \text{nonpenetrating} \\ L \;;\; 0 \le L \le R(E_{inc}), & \text{penetrating,} \end{cases} \tag{3.1}$$

where q_e is the electron charge, ρ_m is the mass density of the material, $Q_{e\gamma}$ is the average conversion efficiency of excited electrons to photons (of various wavelengths), and L is the sample thickness. The dose rate (absorbed power per unit mass), $\dot{D}$, in a sample volume [$R(E_{inc})$ times the beam area] is given by

$$\dot{D}(J_{inc}, E_{inc}) = \frac{J_{inc}E_{inc}}{q_e \rho_m R(E_{inc})}[1 - \eta(E_{inc})], \quad (3.2)$$

where $\eta(E_b)$ is the contribution of backscattered yield. $\dot{D}_{sat}$ is the material-dependent saturation dose rate. The exponential terms in Eq 3.1 account for temperature dependence (Jensen and Dennison, 2015). The last two λ-dependent terms correct for photon absorption within the luminescent material and reflection from any underlying coating (Dennison *et al*., 2012). A more detailed discussion of the model is given in (Dennison *et al*., 2013). This work focuses on the dependence of spectral radiance on J_{inc}, E_{inc}, and the range of the deposited electrons, $R(E_{inc})$.

The dependence of the spectral radiance on incident current density, J_{inc}, in Eq 3.1 is through the dependence on dose rate; $I_\gamma(J_{inc}) \propto \dot{D}(J_{inc})/[D(\dot{J}_{inc}) + \dot{D}_{sat}] \propto J_{inc}/[J_{inc} + J_{sat}]$. At low dose rates ($\dot{D} \ll \dot{D}_{sat}$), I_γ is linearly proportional to J_{inc}. At higher current densities ($\dot{D} \gg \dot{D}_{sat}$), saturation occurs when trap states fill, limiting the number of states into which electrons can decay; I_γ approaches a constant material-specific saturation intensity. Such saturation effects, at increasing current densities and fixed incident energies, have been reported for disordered SiO_2 (Jensen and Dennison, 2015), nanodielectric carbon-loaded polyimide (Jensen *et al*., 2013a), cynate ester/graphite fiber composites (Roth *et al*., 2009), and bisphenol/amine epoxy (Dennison *et al*., 2013; Dekany *et al*., 2015).

The energy dependence of the spectral radiance is more complicated, due to the energy-dependent penetration depth or range, $R(E_{inc})$, in Eq 3.2. For nonpenetrating radiation—where the energy-dependent penetration depth or range, $R(E_{inc})$, is less than

the film thickness L—all incident power is absorbed in the material. At low incident power, both $\dot{D}$ and I_γ are linearly proportional to the incident energy and power density, $(J_{inc}E_{inc}/q_e)$. At higher incident power, both $\dot{D}$ and I_γ exhibit saturation effects for increasing energy and fixed current density. For penetrating radiation—where $R(E_{inc}) > L$—the absorbed power is reduced by a factor of $[L/R(E_{inc})]$ (Wilson and Dennison, 2012) leading to a similar dependence for I_γ. FIG. 3.1 shows the range and dose for select disordered materials as functions of incident energy.

An energy-dependent correction to the incident flux, $J_{inc}[1 - \eta(E_{inc})]$, is also included in Eq 3.2 to account for quasi-elastic backscattered electrons that do not deposit substantial energy; $\eta(E_{inc})$ is the backscattered electron yield (Dennison *et al.*, 2012). Most of the time, this correction is small and weakly dependent on energy. For biased samples, or when excess charge is stored in the trap states, a surface voltage, V_s , results

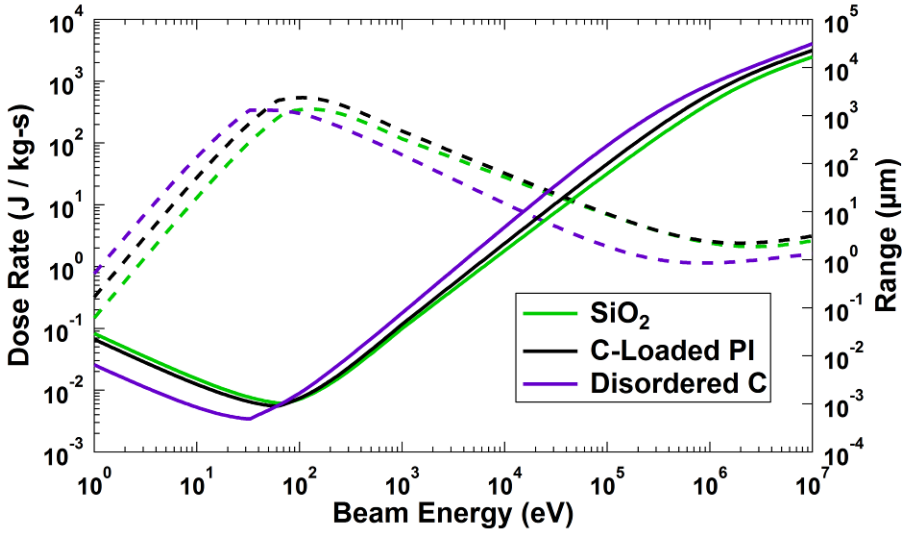

FIG. 3.1. Range (solid curves) and dose rate (dashed curves) of three disordered materials (SiO_2, carbon-loaded polyimide, and graphitic amorphous carbon) as a function of incident electron energy using calculation methods and the continuous slow-down approximation described in Wilson and Dennison, 2012.

and E_{inc} is replaced everywhere in Eqs 3.1 and 3.2 by the landing energy, $(E_{inc} - q_e V_s)$.

3.3. Variation with Energy and Penetration Depth

The energy dependence of CL scales as a saturation function of the dose rate [Eq 3.1]. For nonpenetrating radiation, the dose rate [Eq 3.2] scales linearly with energy with a small, usually negligible, correction term for the energy dependence of the electron backscatter yield. FIG. 3.2 shows spectral radiance versus incident energy curves for two bulk materials, cynate ester/graphite fiber composite (red circle) (Roth *et al*., 2009), and bisphenol/amine epoxy (blue triangles) (Dekany *et al*., 2015), where the sample is thick enough that all the incident electrons are deposited. These increase linearly with energy

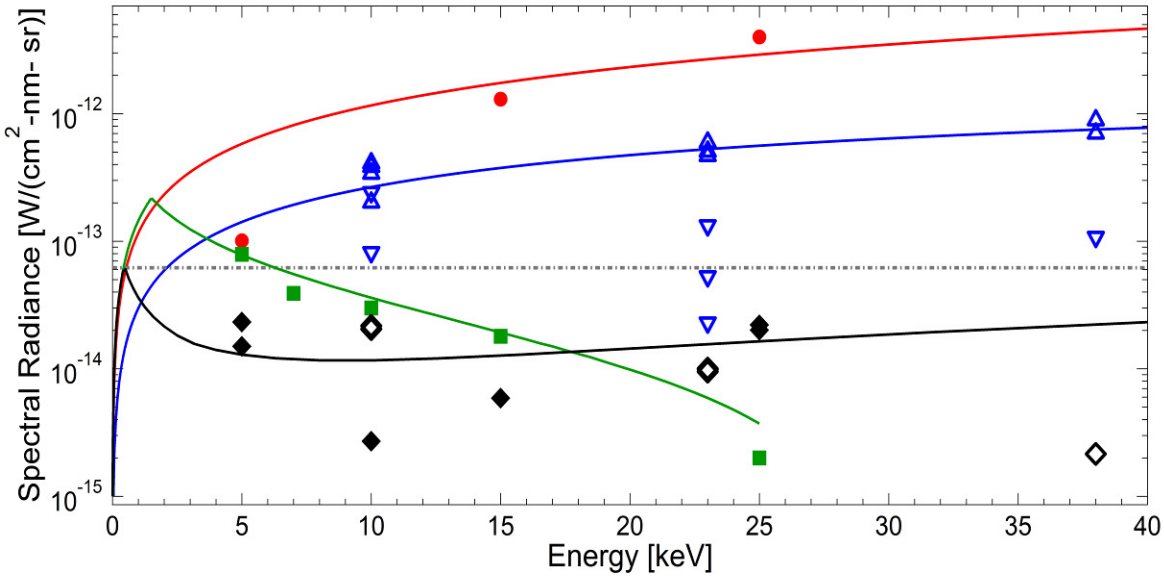

FIG. 3.2. Absolute cathodoluminescent spectral radiance versus incident electron energy of four materials, scaled to 10 nA/cm^2 electron current density. The plot shows data for SiO_2-coated mirror (green square) (Jensen *et al*., 2013b; Jensen and Dennison, 2014a), carbon-loaded polyimide (black diamonds) (Dennison *et al*., 2013; Jensen *et al*., 2013a), cynate ester/graphite fiber composite (red circle) (Roth *et al*., 2009), and bisphenol/amine epoxy (blue triangles) (Dennison *et al*., 2013b; Dekany *et al*., 2015). Data were taken with the CCD video camera at USU (solid symbols) and MSFC (open symbols). Fits are based on Eqs 3.1 and 3.2. The approximate level of the zodiacal background stray light intensity at 863 nm is shown for comparison (dashed grey line) (Leinert *et al*., 1997).

at low incident power density, but reach saturation limits at higher power densities (~10^3 $\mu W/cm^2$ for the cynate ester and ~230 $\mu W/cm^2$ (±70%) for bisphenol materials). The bisphenol data fit by the linear curve in FIG. 3.2 (blue triangles) does not show appreciable saturation, while other data (blue inverted triangles) shows significant saturation effects. The saturated spectral radiance curve (blue curve, with a saturation power density of 360 $\mu W/cm^2$ (±30%)) taken after the electron beam is turned on and after the sample has reached equilibrium deviates noticeably above ~50 $\mu W/cm^2$ from the linear spectral radiance curve (green curve) taken immediately after the electron beam is turned on and before saturation is reached.

For thin films, such as the ~60 nm SiO_2 optical coating in FIG. 3.2 (green curve), incident electrons above a threshold energy (~1.2 keV; FIG. 3.1) are able to penetrate all the way through the material. For energies above this penetrating dose rate, power deposition decreases with increasing energy, so the spectral radiance also decreases. Radiance from thicker SiO_2 layers is found to increase linearly to higher energies and at higher dose rates, exhibit saturation effects (Jensen and Dennison, 2014a).

With composite materials, such as the carbon-loaded polyimide, the relationship between energy and CL intensity is more complicated. The black curve in FIG. 3.2 is a linear superposition with ~88% of a penetrating curve (Dekany *et al*., 2015) (10 nm thickness, with ~350 eV penetration energy), which models thin polyimide layers above carbon particles and ~12% of a nonpenetrating curve (2 μm thickness, with a penetration energy equal to the incident energy of ~10 keV), which models thick polyimide regions between the carbon particles. The relative surface areas of thin (~19%) and thick (~81%) polyimide regions determined with scanning electron microscopy are consistent with

these estimates (Peterson and Dennison, 2013). Even such a simple bimodal distribution of polyimide thicknesses predicts the relatively flat energy dependence of the spectral radiance curve observed at higher energies. A similar effect is seen qualitatively in FIG. 3.2(f) of the cynate ester/graphite fiber composite sample (Dekany *et al*., 2015). Thicker regions of epoxy are lighter, while the thinner epoxy layers over graphite fibers are more intense and brighter blue in color.

3.4. Materials Comparison

As the list of spacecraft materials tested at USU became numerous, it became clear some level of verification of these tests needed to be conducted. As a result, CL tests were done using actual JWST onboard materials, such as carbon-loaded polyimide. Measurements were conducted at two independent facilities: the Environment Effects Laboratory at NASA MSFC and the Space Environment Effects Materials (SEEM) test facility at USU.

USU testing used a ~1 m^3 UHV chamber (~10^{-6} Pa) equipped with a high-energy electron gun with a focused beam (5-30 keV at 0.1-1000 nA/cm^2 flux) (Chang *et al*., 2000). Temperatures from ~50 K to ~350 K were used for CL tests (Dekany *et al*., 2014). Samples from <1 cm to ~3 cm diameter were tested. Additional NIR-IR and mid-IR cameras and detectors, UV/VIS/NIR spectrometers, and electron emission measurement capabilities were used for some measurements (Dennison *et al*., 2013).

Additional tests were done at MSFC under similar conditions. These tests used well-characterized, uniform, large-area, approximately normal-incidence, monochromatic electron beams to irradiate tests samples. MSFC testing used a larger ~2 m x 1 m

diameter UHV chamber (~10^{-6} Pa) able to accommodate large (up to 41x41 cm) flight samples. It was equipped with a high-energy electron flood gun (1-100 keV at 1-100 nA/cm^2 flux) with *in situ* FCs positioned on either side of the large sample to monitor the incident beam current [FIG. 3.3(a)]. Temperatures down to ~120 K were attained by mounting samples on an electrically isolated liquid nitrogen reservoir. The samples were in high vacuum conditions, held at fixed temperatures that could be controlled to cryogenic levels. Results presented here used two optical detectors: (i) an image-intensified CCD video camera (Xybion, ISG-780-U-3; ~400-900 nm bandwidth and 830 nm peak wavelength), and (ii) a single lens reflex CCD still camera (Cannon, EOS Rebel

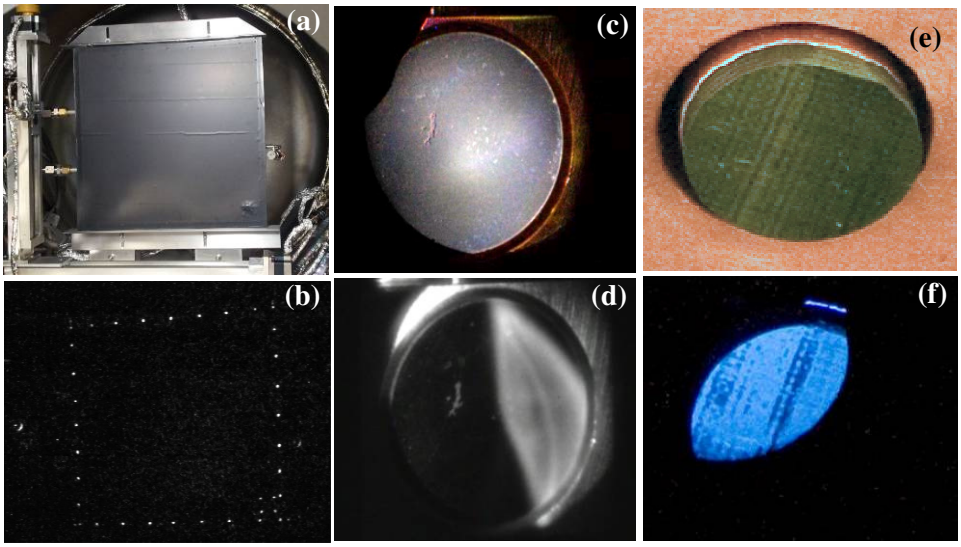

FIG. 3.3. Sample images in ambient light (top) and under electron bombardment (bottom) showing variations in sample composition, size, and facility. (a-b) 41x41 cm sample of carbon-loaded polyimide mounted in the MSFC test chamber, with 36 epoxy glue dots luminescing under electron flux. (c-d) 2.5 cm diameter sample of thin disordered SiO_2 coating on Au-coated mirror mounted in the USU SEEM test chamber. (d) Image with the beam focus adjusted so electrons impinge and cathodoluminescence is evident only on the right side of the sample. (e-f) 1 cm diameter sample of cynate ester/graphite fiber composite at USU. Striations in the images result from the composite fiber structure of the material. (f) Image with the electron beam offset to the top left, limiting cathodoluminescence to this quadrant. (b) and (d) are CCD video frame images; all other images are SLR still color photographs.

XT DS126071; ~390-650 nm bandwidth and 553 nm peak wavelength) (Dennison *et al.*, 2013). The cameras were calibrated on an absolute scale using NIST traceable sources; their detection threshold sensitivities are noted in FIG. 3.4. In addition to the optical detectors, picoammeters measured current through the sample, monitored the mounting stage current, and measured beam currents.

FIG. 3.3 shows some examples of materials tested and CCD video camera and SLR still camera color images of the CL. In FIG. 3.3(d) CL is evident only on the right side of the SiO2 sample, where the beam has been focused. FIG. 3.3(f) of a cynate ester/graphite fiber composite sample shows a uniform circular electron beam offset to

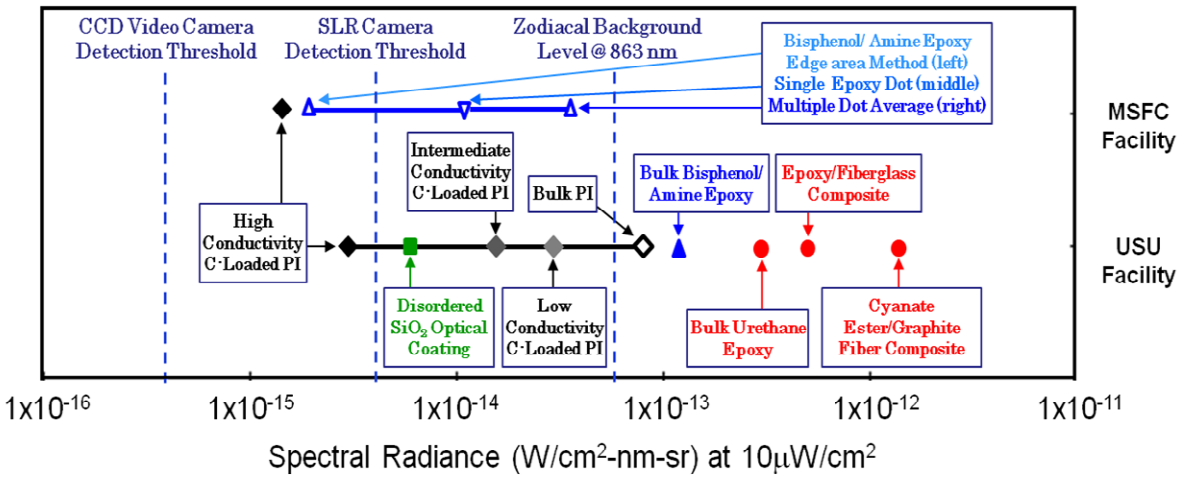

FIG. 3.4. Measured absolute cathodoluminescent intensities for ~10 keV electron bombardment scaled to 10 μW/cm^2, representative of severe space environments. Data acquired using the CCD video camera (863 nm weighted central wavelength and 500 nm bandwidth). The materials shown—in approximate order of increasing intensity—are: three levels of decreasing carbon loading of polyimide from high to low conductivity and bulk polyimide (black squares); disordered SiO_2 optical coatings (green); neat bisphenol/amine and urethane epoxies (blue); and composite resin fiber materials including cyanate ester/ graphite fiber, urethane epoxy/carbon fiber, and epoxy/fiberglass composites (red);. Measurements at the two test facilities are identified at right. Three data analysis methods are compared for bisphenol/amine samples; these range over more than two orders of magnitude, illustrating the need for well-designed test methods. The spectral radiance for the zodiacal background stray light intensity at 863 nm is shown for comparison (dashed blue line) (Leinert *et al.*, 1997), as are the detection thresholds of the cameras at the MSFC facility (Dennison *et al.*, 2013).

the top left, limiting CL to this quadrant.

Measurements at the two test facilities are identified separately in FIG. 3.4. Measurements for similar materials (bisphenol/amine and intermediate conductivity carbon-loaded polyimide samples) show agreement to within a factor of ~2-3. This is reasonable agreement given the differences in sample materials, temperatures, test methods, instrumentation, and electron bombardment conditions for the different tests. However, it also serves as an indication of the uncertainties associated with ground-based testing.

3.4.1. Variations with Materials

FIG. 3.4 shows a comparison of measured absolute CL spectral radiances for different spacecraft materials, which spans approximately three orders of magnitude (Dekany *et al*., 2015). These different results for varied current and keV electron bombardment have been linearly scaled to 10 $\mu W/cm^2$ incident electron power densities, which is representative of severe space environments. The materials tested include: polyimide films, neat urethane and bisphenol/amine epoxy films; bulk and thin optical coatings of disordered SiO_2; several grades of commercially available, high-conductivity, carbon-loaded, polyimide nanodielectric composites; cyanate ester and urethane epoxy resins in graphite fiber and fiberglass composites; and multilayer dielectric/conductor composites. In general terms, we found the relative CL for a given electron flux ranks from lowest to highest intensity for polyimide nanodielectric composites, disordered SiO_2, bulk polyimide, bulk epoxy materials, and epoxy resin composites. Polyimide and carbon-loaded polyimide exhibit relatively weak CL intensities, with the intensity

decreasing with carbon content. As a point of comparison, note that these absolute spectral intensities for isolated samples exposed to electron fluxes comparable to solar wind intensities span the intensity of the zodiacal background in the visible and near infrared wavelength range (vertical dashed line of FIG. 3.4) (Leinert *et al*., 1997); this relative comparison of intensities to the zodiacal background is most important for space-based observatories, where the zodiacal background can be a significant source of external light contamination (Dennison *et al*., 2013). Also note these measured intensities are greater than the scaled CCD video camera detection threshold.

CHAPTER 4

CONCLUSIONS

The conclusion of this thesis provides a summary of the results and proposed future work. In the summary is an overview of the cryostat system and its extensive capabilities. The summary also reviews the extent of the test facilities and recaps the verification of the apparatus with similar tests conducted at other locations. Finally, the future work section contains proposed modifications to the equipment to extend the capabilities.

4.1. Summary of Results

The UHV cryostat system described here has greatly extended the low-temperature capabilities (<40 K to >450 K) to conduct space environment effects tests in the laboratory environment. The versatility of the sample holder design with integrated quick-connect functionality has facilitated other low-temperature sample testing configurations, including those for RIC (Dennison *et al*., 2016) and dark current measurements (Dekany *et al*., 2013). These custom parallel-plate test fixtures allow low-current measurements down to ~1-50 fA at >1000 V and determination of conductivities down to <1·10-21 (Ω-cm)-1 [10] to 5·10-20 (Ω-cm)-1 (Dennison *et al*., 2016). The RIC tests, which lasted for days, required maintaining stable temperature for 10s of hours to allow samples to come to electrical equilibrium (Dennison *et al*., 2016). The constant voltage conductivity tests measured the long-term (many days) decay of dark current conductivities of spacecraft materials at low temperatures (Dekany *et al*., 2013). The RIC and dark current conductivity tests were performed in two different locations with the

cryostat assembly mounted on different vacuum chambers than described in this paper. Finally, the cryostat and the sample holder detailed in this paper will soon be used to study the temperature-dependent behavior of spacecraft materials under electron beam bombardment, including secondary electron emission in juxtaposition with a hemispherical grid retarding field analyzer (Hoffmann, 2010; Hoffmann and Dennison 2012) and surface charging of dielectric materials in combination with a surface voltage probe (Hodges, 2012; Hodges *et al*., 2014).

4.2. Future Work

This cryostat/sample mount is compatible with electron detection capabilities, as well. Preliminary work has been done to incorporate a surface potential probe to the cryostat system by developing a mounting plate compatible with the second cooling stage outer plate (FIG. 4.1). Although the mounting plate was designed for a unique apparatus located in France, care was taken to allow for the adaptation of devices at USU, such as the custom hemispherical grid retarding field analyzer (HGRFA).

The primary detector for emission studies is the USU HGRFA, with a retarding-field analyzer grid system for emitted-electron energy discrimination between backscattered electrons (energies >50 eV) and secondary electrons (energies <50 eV). The HGRFA uses custom, high-speed, high-sensitivity electronics, and charge neutralization capabilities used with <50 pA, <5 μs, $<3 \cdot 10^3$ electrons/pulse pulsed-beam sources permit high-accuracy electron emission measurements of extreme insulators with minimal charging effects (Hoffmann and Dennison, 2012; Dennison *et al*., 2016). *In situ* monitoring of surface voltage, arcing, and luminescence (250 nm to 5000 nm) have also

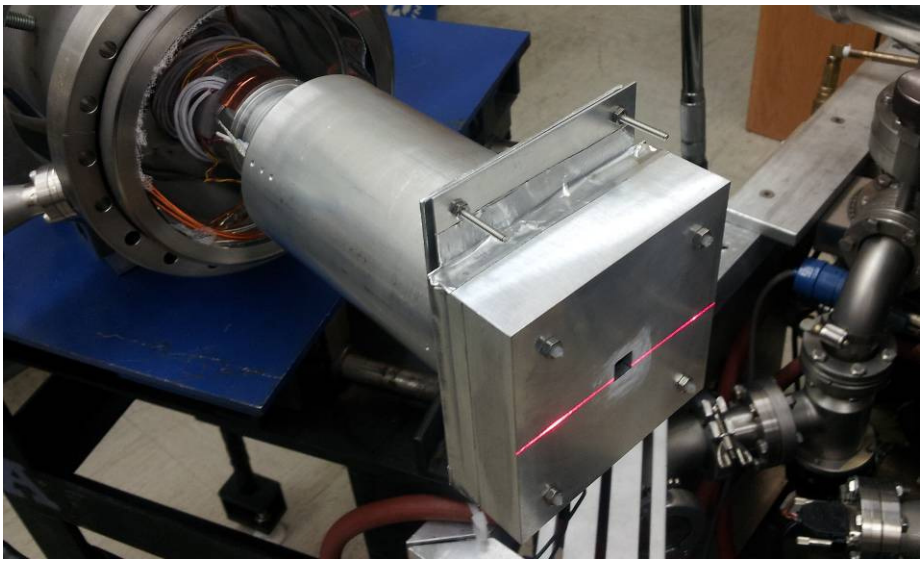

FIG. 4.1. Mounting plate for surface potential probe attached (shown here with the laser) or the plate could be adapted for use with the USU HGRFA. The second cooling stage cylinder can be rotated for fine-tune adjustments.

been added. By ramping the grid bias, energy spectra of the emitted electrons can also be measured using this detector. The HGRFA features a fully encasing hemispherical collector for full capture of emitted electrons, which is particularly well suited and calibrated for absolute yield measurements. The HGRFA can be positioned in front of a single sample mounted at the end of the cryostat with the developed mounting plate with the addition of a mounting bracket. When installing the HGRFA to the cryostat, it is important to align the sample plane with the device's working plane. Fine-tune adjustments are possible by rotating the second cooling stage.

REFERENCES

Chang, W. Y., J. Dennison, N. Nickles, and R. E. Davies, 2000, "Utah State University Ground-Based Test Facility for Study of Electronic Properties of Spacecraft Materials," in *6th Spacecraft Charging and Technology Conference,* Air Force Research Laboratory Science Center, Hanscom Air Force Base, MA.

Dekany J., A. Sim, J. Brunson, and J. R. Dennison, 2013, "Electron Transport Models and Precision Measurements with the Constant Voltage Conductivity Method," IEEE Trans. on Plasma Sci., **41**(12), 3565-3576.

Dekany, J., J. Christensen, J. R. Dennison, A. E. Jensen, G. Wilson, T. Schneider, C. W. Bowers, and R. H. Meloy, 2015, "Variations in Cathodoluminescent Intensity of Spacecraft Materials Exposed to Energetic Electron Bombardment," IEEE Tran. Plasma Science, **43**(11), 3948-3954.

Dekany, J., R. H. Johnson, G. Wilson, A. Evans, and J. R. Dennison, 2014, "Ultrahigh Vacuum Cryostat System for Extended Low Temperature Space Environment Testing," IEEE Trans. on Plasma Sci, **42**, 266.

Dennison, J. R., 2009, "Characterization of Electrical Materials Properties Related to Spacecraft Charging," *Radiation Capabilities for the Europa Jupiter System Missions Instrument Workshop*, Johns Hopkins Applied Physics Laboratory, Laurel, MD, July, 13 pp.

Dennison, J. R., J. Christensen, and J. Dekany, 2016, "Measurements of Intrinsic Electron Emission Yields of High Resistivity Ceramic Materials," in *Proc.* 14th *Spacecraft Charging Technology Conference,* Space Research and Technology Centre of the European Space Agency (ESA/ESTEC), Noordwijk, Netherlands.

Dennison, J. R., A. Evans, G. Wilson, C. W. Bowers, and R. H. Meloy, 2012, "Electron Beam Induced Luminescence of SiO_2 Optical Coatings," in *Conf. on Electrical Insulation and Dielectric Phenomena,* Montreal, Canada.

Dennison, J. R., J. C. Gillespie, A. Andersen, A. E. Jensen, J. Dekany, G. Wilson, A. M. Sim, and R. Hoffmann, 2016, "Synergistic Models of Electron Emission and Transport Measurements of Disordered SiO_2," in *Proc.* 14th *Spacecraft Charging Technology Conference,* Space Research and Technology Centre of the European Space Agency (ESA/ESTEC), Noordwijk, Netherlands.

Dennison, J. R., A. E. Jensen, J. Dekany, G. Wilson, C. W. Bowers, and R. Meloy, 2013, "Diverse Electron-induced Optical Emissions from Space Observatory Materials

at Low Temperatures," in *Proc. SPIE Cryogenic Optical Systems and Instr. Conf.*, **8863**, pp. 88630B1-88630B15.

Guerch, K., J. Dekany, J. R. Dennison, J. Christensen, T. Paulmier, S. Guillemet-Fritsch, and P. Lenormand, 2015, "Cathodoluminescence Studies of Defects in Coated Boron Nitride" J. of Phys. D : Appl. Phys.

Hodges, J., 2012, "*In Situ* Measurements of Electron-Beam-Induced Surface Voltage of Highly Resistive Materials," Master's Thesis (Utah State University).

Hodges, J., A. Sim, J. Dekany, G. Wilson, A. Evans, and J. R. Dennison, 2014, "*In Situ* Surface Voltage Measurements of Dielectrics under Electron Beam Irradiation," IEEE Trans. on Plasma Sci. **42**, 255.

Hoffmann, R., 2010, "Electron-Induced Electron Yields of Uncharged Insulating Materials," Master's Thesis (Utah State University).

Hoffmann, R., and J. R. Dennison, 2012, "Methods to Determine Total Electron-Induced Electron Yields Over Broad Range of Conductive and Nonconductive Materials," IEEE Trans. on Plasma Sci., **40**(2), 298-304.

Hoffmann, R., J. R. Dennison, A. Jensen, and G. Wilson, 2013, "The Correlation Between Radiation Induced Conductivity (RIC) and Electron Beam Induced Luminescence in Disordered SiO_2," in *Proc. 2013 IEEE International Conf. on Solid Dielectrics* (ICSD), Bologna, Italy.

Jensen, A., 2014, " Modeling the Defect Density of States of. Disordered SiO_2 Through Cathodoluminescence," Master's Thesis (Utah State University).

Jensen, A. E., and J. R. Dennison, 2014a, "Defects Density of States Model of Cathodoluminescent Intensity and Spectra of Disordered SiO_2," in *13th Spacecraft Charging Technology Conf.,* Pasadena, CA.

Jensen, A. E., and J. R. Dennison, 2015, "Defects Density of States Model of Cathodoluminescent Intensity and Spectra of Disordered SiO_2," IEEE Tran. Plasma Science, **43**(9), 2925-2932.

Jensen, A., J. R. Dennison, G. Wilson, and J. Dekany, 2013a "Nanodielectric Properties of High Conductivity Carbon-Loaded Polyimide Under Electron-Beam Irradiation," in *Proc. IEEE Intern. Conf. on Solid Dielectrics* (ICSD), Bologna, Italy.

Jensen, A, J. R. Dennison, G. Wilson, J. Dekany, C. W. Bowers, R. H. Meloy, and J. Heaney, 2013b, "Properties of Cathodoluminescence for Cryogenic Applications of SiO_2-based Space Observatory Optics and Coatings," in *Proc. Society of*

Photo-Optical Instrumentation Engineers Cryogenic Optical Systems and Instruments Conference, **8863**, pp. 88630A1-88630A10.

Jensen, A., G. Wilson, J. Dekany, A. Sim, and J. R. Dennison, 2014b, "Low Temperature Cathodoluminescence of Space Observatory Materials," IEEE Trans. on Plasma Sci., **42**(1), 272-277.

Leinert, C., et al., 1997, "The 1997 Reference of Diffuse Night Sky Brightness," Astron. Astrophys. Suppl. Ser., **127**, 1.

Leach, R., and M. Alexander, 1995, "Failures and Anomalies Attributed to Spacecraft Charging," NASA STI/Recon Technical Report N **96**, 11547.

Nickles, N., 2002, "The Role of Band Gap in the Secondary Electron Emission of Small Band Gap Semiconductors: Studies of Graphitic Carbon," Ph.D. Dissertation (Utah State University).

Peterson, K., and J. R. Dennison, 2013, "Atomic Oxygen Modification of the Nanodielectric Surface Composition of Carbon-Loaded Polyimide Composites," in *Am. Phys. Soc. Four Corner Section Meeting*, Denver, CO.

Roth, J., R. Hoffmann, and J. R. Dennison, 2009, "Effects of Radiation Induced Conductivity on Electrostatic Discharge in Insulating Materials," *Proc. 1st AIAA Atmospheric and Space Environments Conf.*, San Antonio, TX.

Sim, A., and J. R. Dennison, 2013, "Comprehensive Theoretical Framework for Modeling Diverse Electron Transport Experiments in Parallel Plate Geometries," AIAA-2013-2827, *5th AIAA Atmospheric and Space Environ. Conf.*, San Diego, CA.

Teyssedre, G., C. Laurent, G. C. Montanari, F. Palmieri, A. See, L. A. Dissado, and J. C. Fothergill, 2001, "Charge Distribution and Electroluminescence in Cross-Linked Polyethylene Under dc Field," J. Phys. D: Appl. Phys., **34**, 2830.

Thomson, C. D., V. Zavyalov, and J. R. Dennison, 2003, "Instrumentation for Studies of Electron Emission and Charging from Insulators," in *Proc. 8th Spacecraft Charging Technology Conference,* NASA Marshall Space Flight Center, Huntsville, AL.

Wilson, G., and J. R. Dennison, 2012, "Approximation of Range in Materials as a Function of Incident Electron Energy," IEEE Trans. on Plasma Sci. **40**, 291.